J. Fluid Mech. (2007), *vol.* 591, *pp.* 321–337.
doi:10.1017/S0022112007008440 Printed in the United Kingdom

Passive wing pitch reversal in insect flight

ATTILA J. BERGOU[1], SHENG XU[2]† AND Z. JANE WANG[2]

[1]Department of Physics, Cornell University, Ithaca, NY 14853, USA

[2]Department of Theoretical and Applied Mechanics, Cornell University, Ithaca, NY 14853 USA

(Received 19 September 2006 and in revised form 7 July 2007)

Wing pitch reversal, the rapid change of angle of attack near stroke transition, represents a difference between hovering with flapping wings and with a continuously rotating blade (e.g. helicopter flight). Although insects have the musculature to control the wing pitch during flight, we show here that aerodynamic and wing inertia forces are sufficient to pitch the wing without the aid of the muscles. We study the passive nature of wing pitching in several observed wing kinematics, including the wing motion of a tethered dragonfly, *Libellula pulchella*, hovering fruitfly, hovering hawkmoth and simplified dragonfly hovering kinematics. To determine whether the pitching is passive, we calculate rotational power about the torsion axis owing to aerodynamic and wing inertial forces. This is done using both direct numerical simulations and quasi-steady fluid force models. We find that, in all the cases studied here, the net rotational power is negative, signifying that the fluid force assists rather than resists the wing pitching. To further understand the generality of these results, we use the quasi-steady force model to analyse the effect of the components of the fluid forces at pitch reversal, and predict the conditions under which the wing pitch reversal is passive. These results suggest the pitching motion of the wings can be passive in insect flight.

1. Introduction

Owing to morphological constraints, insects must reverse the direction of their wing motion periodically. Correspondingly, the wing pitch is also reversed in order to maintain a positive angle of attack during the entire period. At the transition from an up-stroke to a down-stroke, the wing pitch reversal is called pronation, and at the transition from a down-stroke to an up-stroke, it is called supination. In a dragonfly, the wing pitch reversal is primarily responsible for orienting a wing so that it plunges down at a large angle of attack and then returns at a smaller angle of attack. Figure 1 shows snapshots of the wing motion of a tethered dragonfly over one period. Pronation occurs in frames 1–2 and supination can be observed in frames 5–7. In other insects (e.g. fruitflies), the pitch reverses such that the mid-stroke angle of attack is about the same in the back and forth strokes. This sudden wing pitch reversal marks the main difference between hovering using a flapping motion and using a continuously rotating wing. It is therefore of interest to understand whether the pitch reversal requires active muscle control from the insect or whether it can result from a passive mechanism.

† Present address: Department of Mathematics, Southern Methodist University, Dallas, TX 75275, USA.

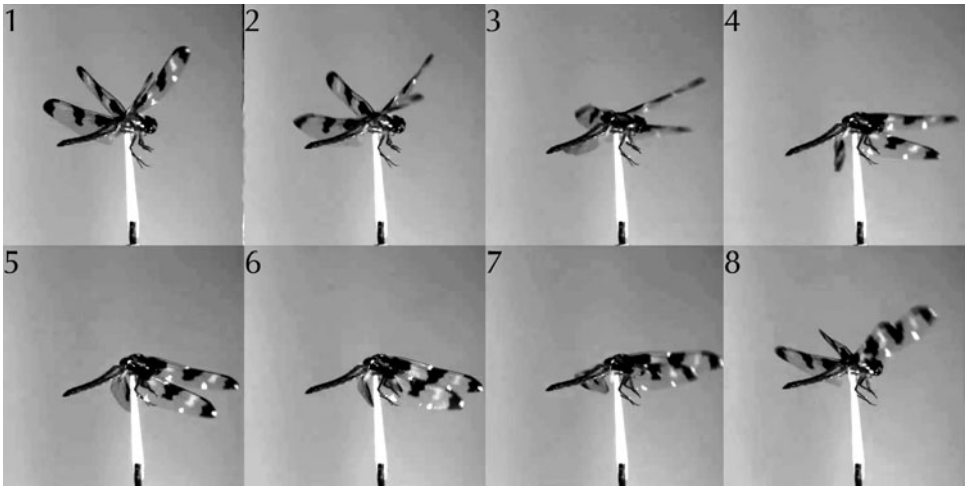

FIGURE 1. Snapshots from the video of tethered dragonfly motion during one period (Russell 2004; Wang & Russell 2007).

It is known that insects are able to modulate the timing of pitch reversal, which implies that muscles can actively control pitching (Ellington 1984; Dickinson, Lehmann & Götz 1993). This may be especially useful during manoeuvring (Dickinson *et al.* 1993). It has been suggested, however, that the torsion axis is positioned so that, for steady flight, aerodynamic forces and wing inertia aid wing pitching (Norberg 1972). The muscle forces that an insect exerts on the wings act through an axis near the leading edge of the wing (Norberg 1972). The wing's centre of mass, however, is behind the leading edge. Therefore, near stroke reversal, a muscle force applied near the leading edge will cause a moment about the centre of mass that will cause it to pitch. From analysis of the inertial forces on the wings of a housefly (Diptera), it has been suggested that wing inertia is sufficient to cause wing pitch reversal (Ennos 1988).

In this paper, we compute the power required by the insect to pitch the wing. We take into account aerodynamic forces on the wing as well as the wing inertia. To compute the aerodynamic power for the observed wing kinematics, we solve the two-dimensional Navier–Stokes equations as well as a simplified quasi-steady force model. We analyse several wing kinematics, including those measured from a tethered dragonfly (Russell 2004; Wang & Russell 2007), as well as published kinematics of a hovering fruitfly (Fry, Sayaman & Dickinson 2005), hovering hawkmoth (Willmott & Ellington 1997*a*), and simplified dragonfly hovering kinematics (Wang 2000). We find that for all the kinematics, no power is required from the insect for wing pitch reversal, thus the wing pitching is passive. We further observe that the rotational power due to aerodynamic forces is comparable to inertial effects in fruitflies and dragonflies. In hawkmoths, the inertial effects become more important. Employing a quasi-steady model, we show that for any kinematics where pitch reversal occurs near stroke reversal, where forces due to wing acceleration and wing rotation dominate those due to velocity, both the aerodynamic and the inertial forces aid the wing pitching. A signature of passive wing pitch reversal is the direction of the torsional wave travelling along the back of the wing during reversal. If it propagates from near the tip to the root, then this suggests that the aerodynamic force, which is maximal near the tip, is responsible for the turning motion. If the wave propagates from the

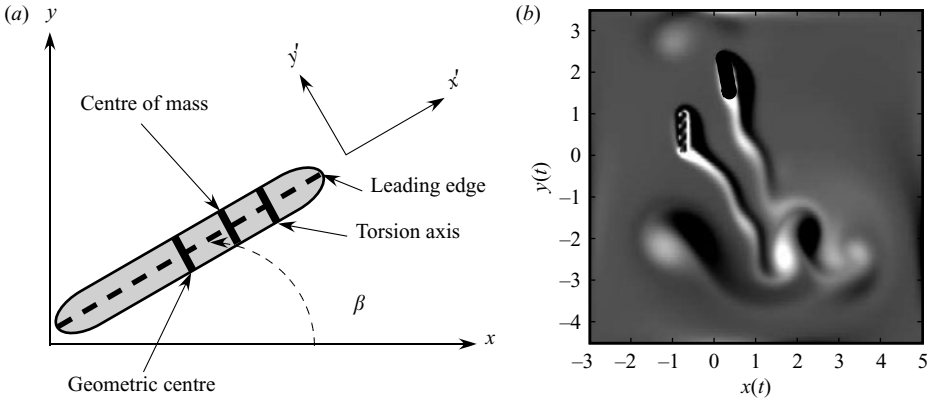

FIGURE 2. (*a*) Two-dimensional coordinate system. The wing chord is shaded in grey. For a dragonfly, the torsion axis and the centre of mass are located at approximately 15 % and 30 % of a chord length behind the leading edge of the wing. (*b*) A snapshot of vorticity field during the flapping period just prior to pronation.

root to tip, then it suggests that the muscle force applied near the root, is turning the wing. We observe a torsional wave travelling from tip to root for the dragonfly wing kinematics, thus providing experimental evidence for our results.

2. Methods

2.1. *Determining passivity*

In order to determine whether the wing pitch reversal is active or passive, we calculate the power required by the insect to produce the observed pitching motion. The pitch is the rotational motion of the wing about the torsion axis, the axis through which the forces produced by the muscles of the insect wing act, and about which forces applied to the wing will generate no moment on the wing (Norberg 1972). Accordingly, in order to determine the power requirements, we calculate the rotational power about this line.

Although the immersed interface method we use for direct numerical simulation is naturally suited for modelling a flexible wing structure, in this paper, we approximate the wing as a rigid plate to calculate two-dimensional forces and power. This is motivated by the observation that the most visible deformation during wing pitch reversal is the twisting along the torsional axis (Song *et al.* 2000). The twisting is mainly caused by the different amounts of wing rotation along the wingspan. This deformation is different from the camber of a clamped plate owing to the forces applied at the two ends. The rigid-plate approximation simplifies analysis and also helps us decouple the effect of the wing camber (Combes & Daniel 2003), from the effect of twisting due to pitching which is our current focus. We will first calculate the rotational power on a two-dimensional rigid wing. By applying blade-element theory to the two-dimensional result, we can qualitatively explain the twisting along the span of the wing. The two-dimensional cross-section of the insect wing is shown in figure 2(*a*). In this model, the angular motion of the three-dimensional wing is described by translation in the $\hat{x}$- and $\hat{y}$-direction, while pitching corresponds to the angle β. The locations of the torsion axis and centre of mass of a dragonfly wing are taken from measurements in Norberg (1972).

Given a set of kinematics, the total power that is exerted by the insect, P_{insect}, can be calculated from,

$$P_{insect} = m\boldsymbol{a}_{cm} \cdot \boldsymbol{v}_{cm} + I_{cm}\ddot{\beta}\dot{\beta} - P_{aerodynamic}, \tag{2.1}$$

where $\boldsymbol{a}_{cm}$ and $\boldsymbol{v}_{cm}$ are the velocity and acceleration of the centre of mass of the wing, m and I_{cm} are the mass and moment of inertia of the wing and $P_{aerodynamic}$ is the rate of work done by the fluid on the wing. The power can be decomposed into rotational and translational components about the torsion axis. The power required by the insect to pitch the wing, P_{rot}, is then

$$P_{rot} = \underbrace{\dot{\beta}d_{cm}(ma_x \sin\beta - ma_y \cos\beta) + I_{cm}\ddot{\beta}\dot{\beta}}_{P^{rot}_{inertial}} \underbrace{-\dot{\beta}d_{gc}(F_x \sin\beta - F_y \cos\beta) - \dot{\beta}\tau}_{-P^{rot}_{aerodynamic}}, \tag{2.2}$$

where d_{cm} is the distance from the centre of mass to the torsion axis, d_{gc} is the distance from the geometric centre of the wing to the torsion axis and F_x, F_y and τ are the aerodynamic forces and torque about the geometric centre of the wing, and the accelerations, a_x and a_y, are at the centre of mass.

2.2. *Immersed interface method*

We solve for the aerodynamic forces and torque in (2.2) by solving the Navier–Stokes equations directly using the immersed interface method, described in Xu & Wang (2006*a*). This is a spatially second-order-accurate method in which the boundary of an object is represented by a singular force that is added as a forcing term to the equation:

$$\frac{\partial \boldsymbol{v}}{\partial t} + \nabla \cdot (\boldsymbol{v}\boldsymbol{v}) = -\nabla p + \frac{1}{Re}\Delta \boldsymbol{v} + \sum_{l=1}^{M} \boldsymbol{F}_l, \tag{2.3}$$

where $\boldsymbol{v}$ and p are the velocity and pressure fields, $\boldsymbol{F}_l$ is the singular force from object l and Re is the Reynolds number for our simulation. The equations in this section are shown in dimensionless form where the velocity scale and length scale are determined by the average wing velocity and flapping amplitude, respectively.

The singular force in (2.3) is computed as

$$\boldsymbol{F} = \oint_{\delta\Omega} \boldsymbol{f}(\alpha, t)\delta(x - X(\alpha, t))\delta(y - Y(\alpha, t))\,\mathrm{d}\alpha, \tag{2.4}$$

where $\delta\Omega$ is an object boundary, X and Y are the coordinates of the boundary, $\boldsymbol{f}$ is the singular force density, and α is a non-dimensional Lagrange parameter. The singular force causes jumps across the boundary in the pressure, derivatives of pressure and derivatives of velocity. Expressions for the jumps, integral to the immersed interface method, were derived in Xu & Wang (2006*b*). The singular force density necessary to enforce the prescribed motion of the wings is calculated by a spring model analogous to that described in Xu & Wang (2006*a*).

The Navier–Stokes equations are solved in primitive variables on a MAC grid in pressure Poisson form. Forward-time integration is done using a fourth-order Runge–Kutta method as described in Xu & Wang (2006*a*). The actual dragonfly wing motion occurs at $Re = O(10^3)$. However, as noted in Russell (2004), the aerodynamics are insensitive to Re above $Re = 200$. Figure 2(*b*) is a snapshot of the resulting vorticity field at $Re \approx 250$. For these simulations, we enclose the wings in an 8×8 chord length rigid box, for which a sufficiently accurate approximation of the pressure boundary condition can be derived (Xu & Wang 2006*b*). The wings are modelled as 6 : 1 aspect

ratio rounded rectangles. The qualitative result, that large negative peaks occur in figure 5 indicating that pitch reversal is passive, is independent of the particular shape of the wing.

We tested the algorithm extensively to ensure the accuracy of our results. We performed both spatial and temporal convergence testing and found that a 256×256 grid with $dt = 5 \times 10^{-4}$ sufficiently resolves the flow. The truncation of the domain is also found not to affect our results significantly.

The aerodynamic force about the geometric centre of the wing is given by,

$$\boldsymbol{F} = -\oint_{\delta\Omega} \boldsymbol{f}\,\mathrm{d}\alpha + S\frac{\mathrm{d}\boldsymbol{u}_T}{\mathrm{d}t}, \tag{2.5}$$

where S is the area enclosed by the wing boundary, $\boldsymbol{u}_T$ is the translational velocity of the wing, and $\boldsymbol{f}, \alpha$ are defined above.

The rate of work done by the fluid on the wing can be computed as

$$P = \oint_{\delta\Omega} \sigma_{ij}^{+} u_i n_j \mathrm{d}s, \tag{2.6}$$

where σ_{ij}^{+} is the stress tensor on the outer surface of the wing boundary, and n_j is the outward-pointing surface-normal vector. From force balance (Xu & Wang 2006*b*), the jump condition for the stress tensor satisfies

$$[\sigma_{ij}]n_j = (\sigma_{ij}^{+} - \sigma_{ij}^{-})n_j = -\frac{f_i}{J}, \tag{2.7}$$

where $J = \mathrm{d}s/\mathrm{d}\alpha$ is the Jacobian, and σ_{ij}^{-} is the stress tensor on the inner surface of the wing boundary. Noting that $\mathrm{d}s = J\mathrm{d}\alpha$, we can combine (2.6) and (2.7) to

$$\begin{aligned} P &= -\oint_{\delta\Omega} \boldsymbol{f}\cdot\boldsymbol{u}\,\mathrm{d}\alpha + \int_{\delta\Omega} \sigma_{ij}^{-} u_i n_j \mathrm{d}s \\ &= -\oint_{\delta\Omega} \boldsymbol{f}\cdot\boldsymbol{u}\,\mathrm{d}\alpha + \frac{\mathrm{d}K}{\mathrm{d}t} + \frac{1}{Re}\int_{\Omega}\left(\frac{\partial u_i}{\partial x_j}\frac{\partial u_i}{\partial x_j} + \frac{\partial u_j}{\partial x_i}\frac{\partial u_i}{\partial x_j}\right)\mathrm{d}A \\ &\approx -\oint_{\delta\Omega} \boldsymbol{f}\cdot\boldsymbol{u}\,\mathrm{d}\alpha + \frac{\mathrm{d}K}{\mathrm{d}t}, \end{aligned} \tag{2.8}$$

where K is the total kinetic energy in the region Ω enclosed by the wing boundary. The term associated with dissipation is proportional to $1/Re$, and is dropped because for our calculations it is approximately 0.4 % of the size of the other terms.

The torque about the wing centroid can be calculated similarly to the power by

$$\begin{aligned} \tau &= \oint_{\delta\Omega} \epsilon_{ij} r_i \sigma_{jk}^{+} n_k \,\mathrm{d}s \\ &= -\oint_{\delta\Omega} \epsilon_{ij} r_i f_j \,\mathrm{d}\alpha + \frac{\mathrm{d}}{\mathrm{d}t}\int_{\Omega} \epsilon_{ij} r_i u_j \,\mathrm{d}A, \end{aligned} \tag{2.9}$$

where ϵ_{ij} is the two-dimensional Levi–Civita symbol, and r_i is the vector from the centroid of the wing to its boundary.

2.3. *Quasi-steady model of aerodynamic forces*

For an insight into the interplay of forces that exist during the wing pitch reversal, we also study the wing motion using a quasi-steady model. Previous studies have compared the instantaneous force in hovering flight to quasi-steady models (Sane & Dickinson 2002; Wang, Birch & Dickinson 2004). We use the force model developed

to study fluttering and tumbling plates in fluids (Pesavento & Wang 2004; Andersen, Pesavento & Wang 2005*a*, *b*).

We calculate aerodynamic force, $\boldsymbol{F}$, and torque, τ, from a wing motion using,

$$F_{x'} = -m_{11}\dot{v}_{x'} + m_{22}\dot{\beta}v_{y'} - \rho_f \Gamma v_{y'} - F^v_{x'}, \tag{2.10a}$$

$$F_{y'} = -m_{22}\dot{v}_{y'} - m_{11}\dot{\beta}v_{x'} + \rho_f \Gamma v_{x'} - F^v_{y'}, \tag{2.10b}$$

$$\tau = -I_a\ddot{\beta} + (m_{11} - m_{22})v_{x'}v_{y'} - \tau^v, \tag{2.10c}$$

where v is the wing velocity, I is the moment of inertia, m_{11}, m_{22} and I_a are the coefficients of added mass and moment of inertia, Γ is the circulation, and $\boldsymbol{F}^v$, τ^v are the dissipative forces and torque, respectively. The added mass coefficients, m_{11}, m_{22} and I_a, are determined by taking the average values for the inscribed and circumscribed ellipses around the wing. For an ellipse with semi-major axis a, semi-minor axis b, $m_{11} = \pi\rho_f b^2$, $m_{22} = \pi\rho_f a^2$ and $I_a = (1/8)\pi\rho_f(a^2 - b^2)$ (Sedov 1965). Subscripts x' and y' above denote components in the x' and y' directions, and β is the orientation of the wing (figure 2*a*). The primed coordinate system in the above equations, as defined in figure 2(*a*), is co-rotating with the wing.

The circulation, Γ, is calculated from,

$$\Gamma = -2C_T d_{le}\frac{v_{x'}v_{y'}}{|\boldsymbol{v}|} + 2C_R d_{le}^2\dot{\beta}, \tag{2.11}$$

where C_T and C_R are dimensionless constants, and d_{le} is the distance from the geometric centre of the wing to the leading edge. The term involving C_T is associated with the translational circulation, while the term involving C_R is the rotational circulation, their specific values are discussed below. The dissipative force, $\boldsymbol{F}^v$, and the dissipative torque, τ^v, are calculated from

$$\boldsymbol{F}^v = \rho_f d_{le}\left(A|\boldsymbol{v}| - B\frac{v_{x'}^2 - v_{y'}^2}{|\boldsymbol{v}|}\right)\boldsymbol{v}, \tag{2.12a}$$

$$\tau^v = \pi\rho_f d_{le}^4\left(\frac{1}{T}\mu_1 + \mu_2|\dot{\beta}|\right)\dot{\beta}, \tag{2.12b}$$

where T is the flapping period and the dimensionless constants A, B, μ_1 and μ_2 are Reynolds-number dependent. The rotational power is then calculated by making use of (2.2).

We find that the predictions using the quasi-steady model closely match those from the direct simulations. There are two notable exceptions to this. First, the torque about the wing centroid is poorly modelled by (2.10*c*). However, given the small magnitude of the torque, it has a very small contribution to P_{rot} (equation (2.2)) and does not affect our qualitative results. Also, both wings generate a net downward jet that is not present in the quasi-steady model. Significant discrepancies between the quasi-steady model and direct simulations coincide with the wings crossing this jet near supination. These effects are further discussed in the Appendix. In figure 6, $P^{rot}_{aerodynamic}$ is compared between direct simulations and the quasi-steady model. As can be seen in the figure, the peaks in the quasi-steady model have the same sign as in the direct simulations. Since we are mainly interested in the sign of these peaks when determining the passive nature of the wing pitching, we will make use of this quasi-steady model in our general analysis in § 5.

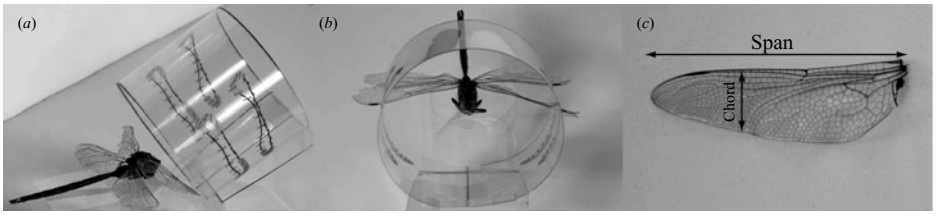

FIGURE 3. Illustration of the three-dimensional to two-dimensional conversion of the dragonfly wing kinematics. (*a*), (*b*) A three-dimensional image of the dragonfly with the two-dimensional projection cylinder. (*c*) The two-dimensional wing with the slices superimposed on them.

2.4. *Dragonfly wing kinematics*

We use the tethered dragonfly wing kinematics measured in Russell (2004) and Wang & Russell (2007). In order to obtain the motion in three dimensions using a single camera, a mirror was placed near the dragonfly. Both the insect and the reflection were recorded using a high-speed camera at 1500 frames s^{-1}. In figure 1, we can see snapshots of the captured wing motion reproduced from Russell (2004) and Wang & Russell (2007). From the video, three-dimensional kinematics were reconstructed using three marked points on the wings for 5 beats of the insects wing. This was done by treating the wings as rigid bodies, ignoring any deformation.

The two pairs of wings move symmetrically and the wing interaction between the two sides is negligible owing to the small stroke angle, we therefore simulate a pair of wings on one side. As mentioned above, we simulate a two-dimensional cross-section. As shown in figure 3, the stroke-planes of the fore- and hind-wings are nearly parallel, oriented at 37° from the vertical. As a result of this, a single cylinder can be aligned such that the axis is perpendicular to both stroke planes. To make use of this for the two-dimensional projection, we take such a cylinder with a radius of two-thirds of the wingspan of the forewing, and use its intersection with the leading edge of each wing to determine the trace of each wing on the cylinder. We convert to Cartesian coordinates by unwrapping the cylinder about the mid-stroke and defining the two-dimensional coordinate system so that $\hat{y}$ corresponds to the vertical direction. Making use of a second intersection point of the wing with the cylinder, we additionally calculate the pitching angle in the two-dimensional coordinate system. To avoid varying the chord length throughout the motion, a constant chord length is maintained and wing position and orientation are determined by the leading-edge intersection of the wing and the pitching angle determined from the second intersection point, respectively. This corresponds, approximately, to taking the two-dimensional cross-section of the wing shown in figure 3(*c*).

The resulting motion is parameterized by the position of the centre of the wing, $x(t)$ and $y(t)$, and the angular orientation of the wing, $\beta(t)$, as defined figure 2(*a*). The average two-dimensional stroke is given by fitting the resulting wing kinematics with an 8 parameter Fourier series to each of $x(t)$, $y(t)$ and $\beta(t)$. The resulting two-dimensional kinematics, the unwrapped motion of the wings, are shown in figures 4(*a*) and 4(*b*). On these figures, we also see the regions of pronation and supination, which are found by analysing the pitching velocity of the wing, $\dot{\beta}$, shown in figures 4(*b*) and 4(*d*).

3. Passive wing rotation in dragonfly flight

In figure 5, we show the rotational power about the torsion axis as a function of time for the fore- and hind-wings, respectively. These are calculated using (2.2)

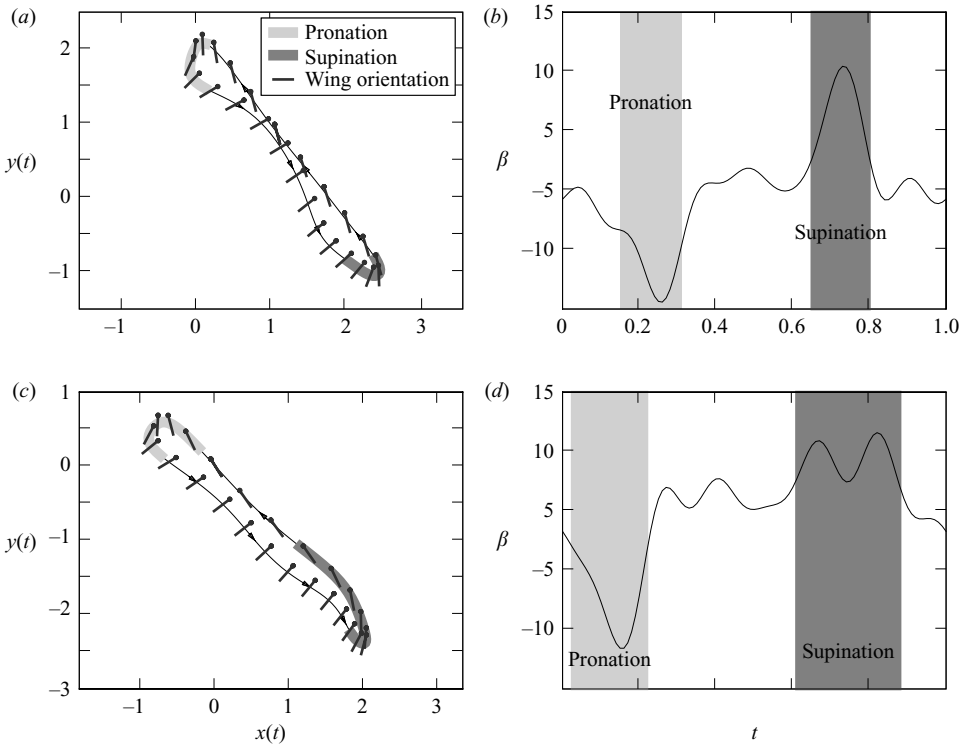

FIGURE 4. Projected motion and angular velocity of a fore- ((*a*) and (*b*), respectively) and a hindwing ((*c*) and (*d*), respectively). In (*a*) and (*c*), the lines indicate snapshots of the angular orientation of the wing (for clarity, line lengths are scaled to 40 % of the actual chord length of the wing). The leading edge of the wing is denoted by the dot. Lengths are in units of chord length, and time in units of flapping period.

for 50 wing strokes and then averaged. Shown are both the contribution from the aerodynamics and the wing inertia. During both pronation and supination, P_{rot} has strong negative peaks that are greater in magnitude during pronation than during supination. The negative peaks indicate that the fluid, by doing work on the wings, actually aids, rather than resists, the wing pitch reversal. This shows that the wing pitch reversal is passive. Both inertial and aerodynamic effects have a tendency to pitch the wing in the proper direction, but in this case, aerodynamic effects dominate.

To further quantify $P^{rot}_{aerodynamic}$, we analyse it using the quasi-steady components found in (2.10*c*). Results are shown in figure 7. $P^{rot}_{aerodynamic}$, as predicted by the quasi-steady model, is insensitive to the exact values of the quasi-steady parameters except for C_R. We therefore use $A = 1.4$, $B = 1.0$, $C_T = 1.2$, $\mu_1 = 0.2$ and $\mu_2 = 0.2$ as in Andersen *et al.* (2005*b*). C_R is determined by minimizing the difference between the quasi-steady and computational fluid dynamics (CFD) results (figure 6).

In figure 7, we see that for both wings, the added mass term dominates all other terms at both pronation and supination. The next dominant term is the rotational circulation term which aids passivity at pronation of the wings and opposes it at supination. The dissipative and rotational circulation terms play only minor roles in wing pitch reversal. However, they tend to oppose wing pitch reversal at the beginning of pronation and supination and aid it in the latter half of it. We therefore see that for the dragonfly kinematics, the passivity of wing pitch reversal is determined, to a large

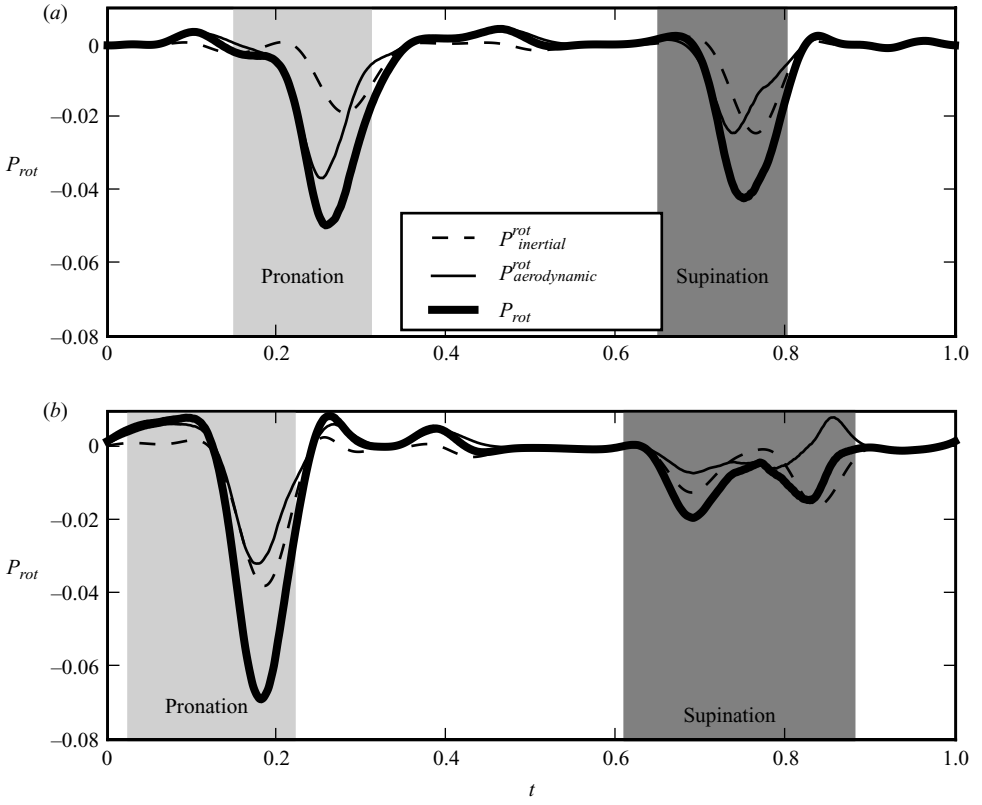

FIGURE 5. The averaged values of P_{rot} for the fore- (*a*) and hind- (*b*) wings as a function of time Pronation and supination are at marked regions. The average value is taken over 50 periods. Also shown are $-P^{rot}_{aerodynamic}$ and $P^{rot}_{inertial}$ from (2.2). Time is in the unit of the flapping period, and P_{rot} dimensions, power per unit length, in the unit of the ratio of the weight of the insect and the time scale.

extent, by added mass and rotational circulation effects, with other terms playing a minor, but discernible, role.

4. Other cases of passive wing pitch reversal

To see whether the above described passive mechanism for wing pitch reversal occurs in other insects, we analyse kinematics for a hovering fruitfly (Fry *et al.* 2005), hovering hawkmoth (Willmott & Ellington 1997*a*), and simplified dragonfly hovering kinematics (Wang 2000). As with the dragonfly, we calculate P_{rot} using (2.2) for a chordwise cross-section of the wing at 66 % the wingspan. In order to model aerodynamic forces, we use the quasi-steady model from (2.10*c*). For the simplified hovering kinematics, the morphological parameters of the dragonfly studied in the previous section are used. For the fruitlfy and hawkmoth, actual morphology of the insects is employed (Willmott & Ellington 1997*b*; Fry *et al.* 2005).

Results for P_{rot} along with each wing motion are shown in figure 8. For each of the kinematics, we see similar results to the dragonfly kinematics. Large negative peaks occur close to the wing pitch reversal, which is nearly coincidental with stroke reversal. Because of the relatively light wings of dragonflies and fruitflies (figures 8*a* and 8*e*), the aerodynamic component of P_{rot} is comparable to the inertial one. For

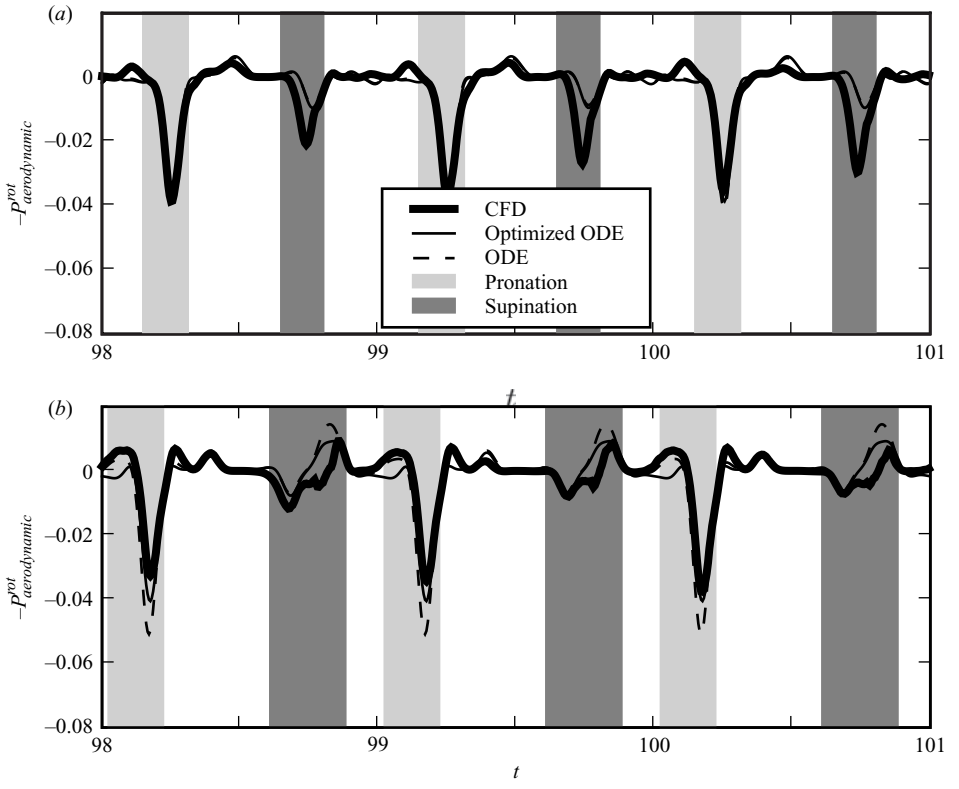

FIGURE 6. Comparison of $-P^{rot}_{aerodynamic}$ calculated using CFD and quasi-steady models for the fore- (*a*) and hindwing (*b*), respectively. The parameters in the quasi-steady model are $A = 1.4$, $B = 1.0$, $C_T = 1.2$, $\mu_1 = 0.2$ and $\mu_2 = 0.2$, as in Andersen *et al.* (2005*b*). C_R is determined by minimizing the difference between the quasi-steady and CFD results. $C_R = 2.58$ for the forewing and 0.90 for the hindwing. The units of time and $P^{rot}_{aerodynamic}$ are the same as in figure 5.

the hawkmoth, however, the inertial component becomes dominant. This is expected, as the hawkmoth has a large wing mass relative to its body mass.

5. Quasi-steady analysis of wing pitch reversal

The fact that passive wing pitch reversal is observed for these different wing kinematics suggests the need for a general explanation. The passive pitching can be intuitively explained as follows. When the wing decelerates prior to stroke reversal, the fluid continues to move forward and pushes the centre of the wing forward causing it to rotate about the torsion axis. This is the added-mass effect. As the wing continues to pitch after stroke reversal, lift, drag and added mass forces on the wing will all be directed in a way that will cause pitch reversal to occur passively. Below, we analyse the relative importance of these terms in the framework of the quasi-steady model. We do this by inspecting the components in the quasi-steady expression for P_{rot} term by term.

If the wing is thin, $b/a \ll 1$, then the added mass coefficients can be simplified as $m_{11} \to 0$, $m_{22} \to m_a$. Hence, we can combine (2.2) and (2.10*c*) to write P_{rot} in the

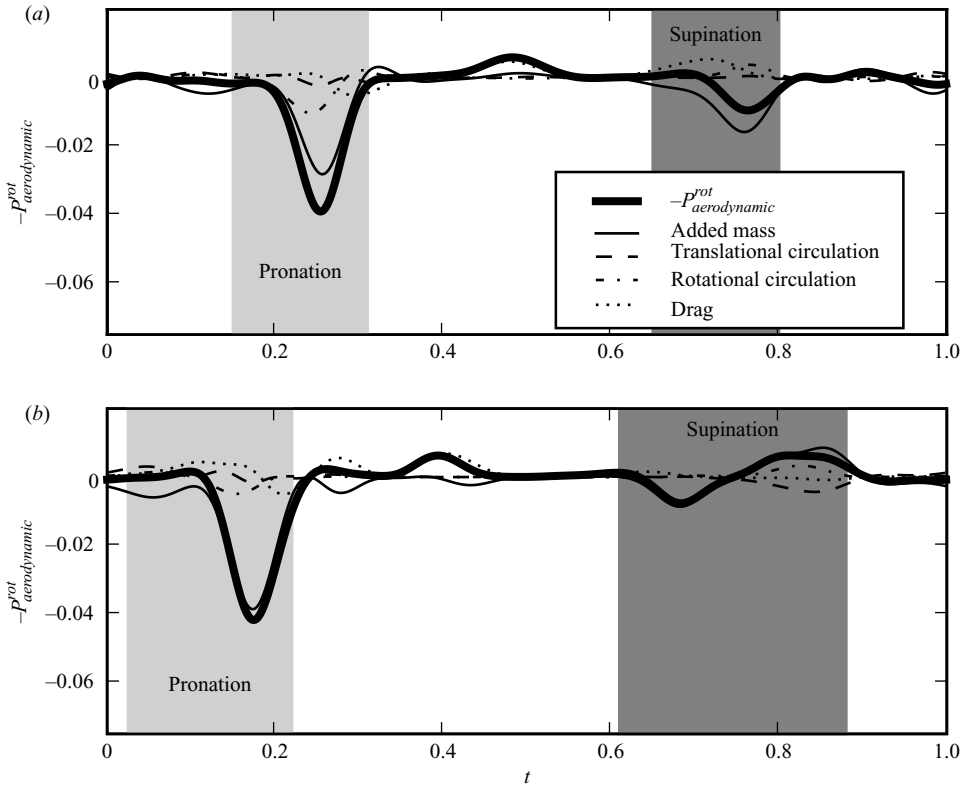

FIGURE 7. $-P^{rot}_{aerodynamic}$ and its components for (*a*) the fore- and (*b*) hind-wings. The units of time and $-P^{rot}_{aerodynamic}$ are the same as in figure 5.

co-rotating coordinate system as,

$$P_{rot} = [\underbrace{(I_{cm} + I_a)\ddot{\beta} - (md_{cm} + m_a d_{gc})a_{y'} + m_a v_{x'} v_{y'}}_{\text{Inertial and added mass}} \underbrace{- d_{gc} F^{v}_{y'} + \tau^{v}}_{\text{Dissipative}} \underbrace{+ \rho_f d_{gc} v_{x'} \Gamma}_{\text{Circulation}}]\dot{\beta}. \quad (5.1)$$

All terms in the equation appear as defined previously. We analyse (5.1) term by term, and seek criteria that, when satisfied, result in wing pitch reversal being passive.

Near stroke reversal, the translational velocity of the wing is small, and therefore drag and circulatory terms will be small because of their velocity dependence. The terms $(I_{cm} + I_a)\ddot{\beta}\dot{\beta} - (md_{cm} + m_a d_{gc})a_{y'}\dot{\beta}$ are independent of velocity and dependent on the acceleration of the wing. Therefore, when pitch reversal occurs in this region added mass and inertial terms dominate P_{rot}. We therefore, first, consider the balance of these two dominant terms. They aid the wing pitch when their sum is negative, this occurs when

$$|\ddot{\beta}| \leqslant \frac{md_{cm} + m_a d_{gc}}{I_{cm} + I_a}|a_{y'}|. \quad (5.2)$$

These terms determine a limit on angular acceleration below which added mass and inertial effects aid in pitch reversal. In figure 9, we plot $\ddot{\beta}^* = (md_{cm} + m_a d_{gc})/(I_{cm} + I_a)|a_{y'}|$ against $|\ddot{\beta}|$ for snapshots in time during the pronation and supination of the previously mentioned wing kinematics. Added mass and inertial effects aid wing pitch reversal for any points that lie below the identity and oppose it otherwise.

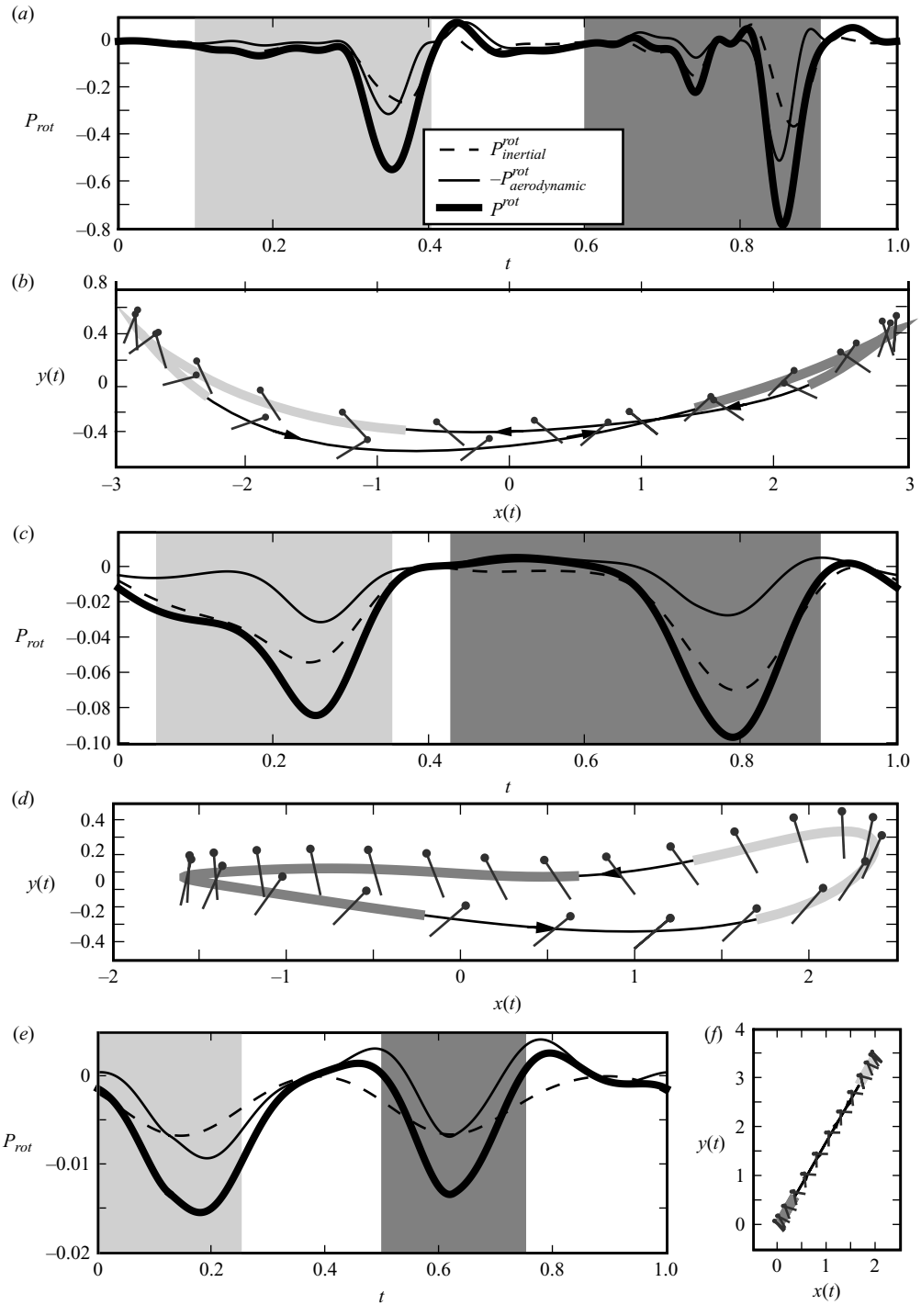

FIGURE 8. Wing motions and quasi-steady P_{rot} for a fruitfly, (*a*)–(*b*), hawkmoth, (*c*)–(*d*), and simplified dragonfly hovering kinematics, (*d*)–(*e*). The units of time and P_{rot} are the same as in figure 5.

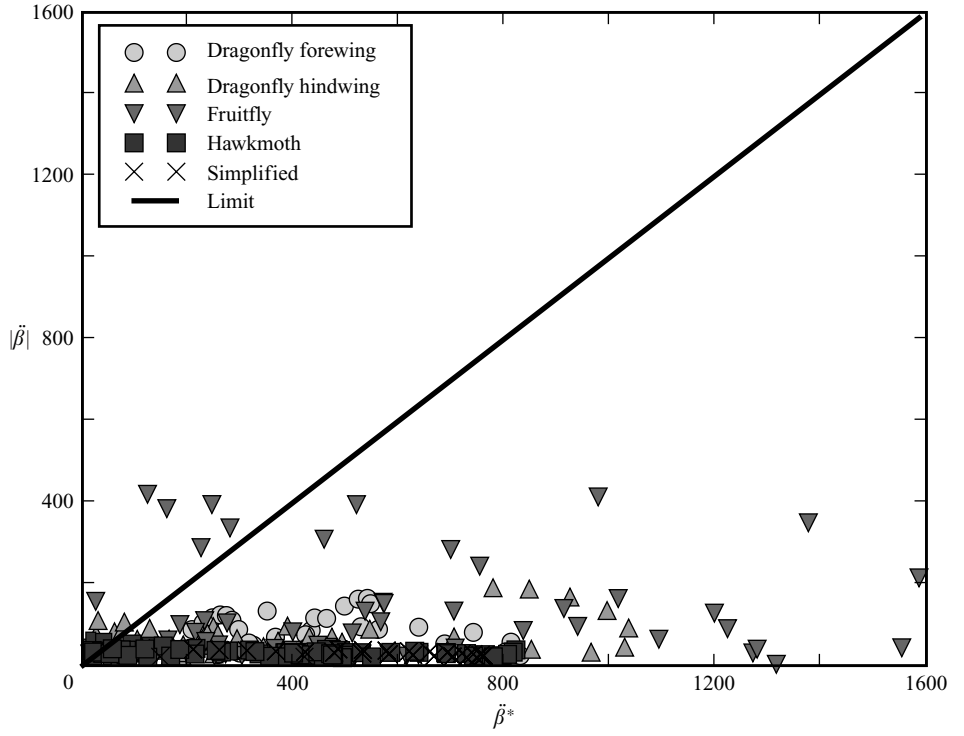

FIGURE 9. Plot of $\ddot{\beta}^* = (md_{cm} + m_a d_{gc})/(I_{cm} + I_a)|a_{y'}|$ against $|\ddot{\beta}|$. The region under the solid line is the limit where inertial and added mass effects aid in wing pitch reversal. The points represent snapshots of the wing kinematics during pronation and supination, i.e. they are values of $\ddot{\beta}(t)$ and $a_{y'}(t)$ for a particular motion at a particular t.

As we see from the figure, most points lie below this line. Therefore, these terms tend to aid pitch reversal during both pronation and supination. The torque due to these terms will pitch the wing such that the leading edge of the wing remains the edge near the torsional axis.

As mentioned, the drag and circulatory terms are small near stroke reversal, however, they can play a role in wing pitching if pitch reversal occurs sufficiently for away from stroke reversal. From (2.12*b*), we see that τ^v will always oppose wing rotation, but is negligible. The other drag term $\boldsymbol{F}^v \propto -|\boldsymbol{v}|\boldsymbol{v}$ will oppose the translational motion of the wing. Therefore, if pitch reversal occurs before stroke reversal, this term opposes pitching, and aids it after stroke reversal. This is in agreement with observations in figure 7.

The circulation term can be decomposed into translational, $P^{rot}_{\Gamma_T}$, and the rotational, $P^{rot}_{\Gamma_R}$, components. Following (2.11),

$$P^{rot}_{\Gamma_T} = -2C_T \rho_f d_{gc} d_{le} \frac{v^2_{x'} v_{y'}}{|\boldsymbol{v}|} \dot{\beta}. \tag{5.3}$$

This term aids pitch reversal when the sign of $v_{y'}$ and $\dot{\beta}$ are the same. This occurs when the trailing edge is rotating away from the direction in which it is moving, as is the case when the wing pitches after stroke reversal. $P^{rot}_{\Gamma_R}$ can be calculated from

$$P^{rot}_{\Gamma_R} = 2C_R \rho_f d_{gc} d^2_{le} v_{x'} \dot{\beta}^2. \tag{5.4}$$

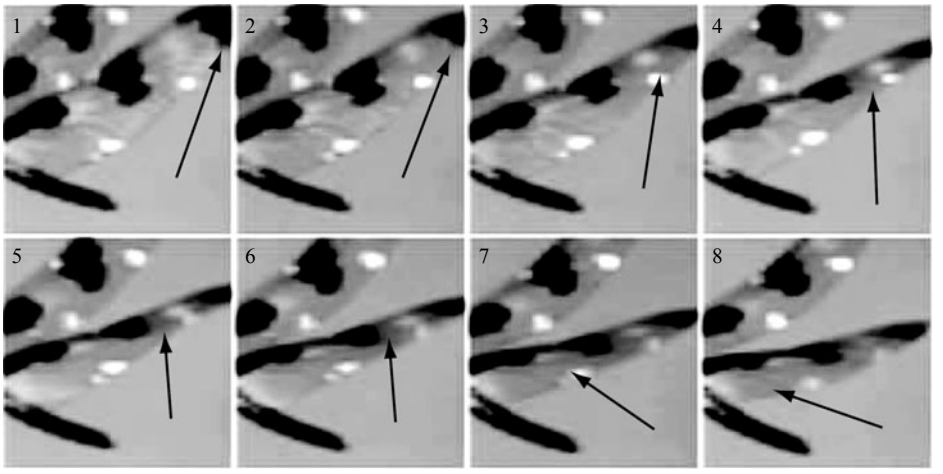

FIGURE 10. Torsional wave propagating along the trailing edge of the wing from base to tip near pronation.

Because of its linear dependence in velocity, its magnitude is typically larger than either drag or translational circulation near wing reversal. The sign of P_Γ is determined by the sign of $v_{x'}$, and opposes wing pitching unless the leading edge is changed from near the torsion axis to the other edge of the wing, which can happen momentarily during the pitch reversal (figure 4). In figure 7, we see that translational circulation aids wing pitch reversal in the latter half of stokes, past stroke reversal. Rotational circulation helps rotate the wing only during pronation, where the leading edge temporarily changes away from the torsion axis. It has a tendency of opposing pitching during supination, where the leading edge remains unchanged.

6. Signature of passive wing reversal

A signature of active versus passive wing pitch reversal is the direction of the torsional wave travelling along the trailing edge of the wing during wing reversal. If the wave propagates from the root to the tip, then the wing pitch reversal is likely to be activated by the muscle, which is applied near the wing root. Such a wave was previously observed in the study of a desert locust, *Schistocerca gregaria* (Weis-Fogh 1973). If, on the other hand, the wave propagates from near the tip to the root, then this suggests that the aerodynamic force, which is maximal near the tip, is responsible for the turning motion. This type of torsional wave was observed in Ennos (1988) for the wings of Diptera during passive wing rotation observed in those insects. In figure 10, we show an enlargement of several frames captured for the tethered dragonfly around the transition from up-stroke to down-stroke. We observe a torsional wave propagating along the trailing edge of the wing, starting near the wing-tip and ending near the wing base. This provides additional evidence for the passive nature of the wing pitching as analysed above.

The torsion along the length of the wing is directly related to the angular rotation of each wing segment comprising it. Using the blade-element approximation and the wing shape of the dragonfly, we determine, for each segment, the torque caused by aerodynamic forces and the insect muscle. The muscle forces act at the torsion axis and are calculated by ensuring that the translational acceleration of the wing matches the wing kinematics, $\boldsymbol{F}_{insect} = m\boldsymbol{a} - \boldsymbol{F}_{aerodynamic}$. The torque about the centre of mass

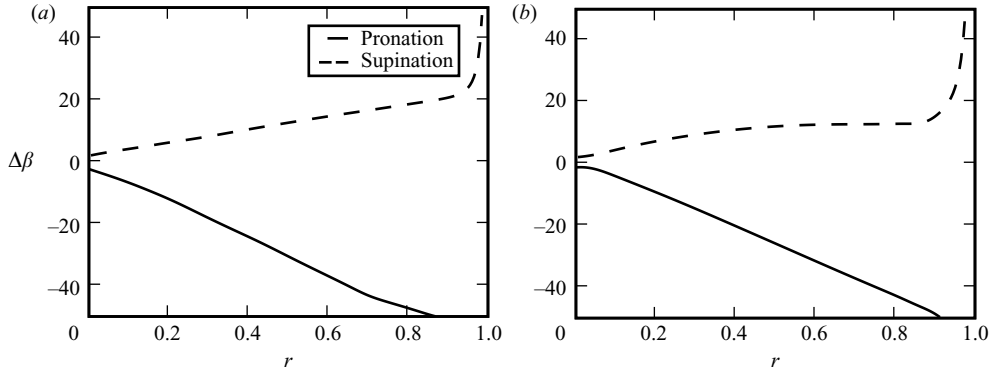

FIGURE 11. Spanwise dependence of $\Delta\beta$ on r, the fractional distance along the span of the wing. $\Delta\beta(r)$ is calculated by integrating the torque about the wing's centre of mass over pronation and supination regions. During pronation, the wing is rotated anticlockwise. During supination, the opposite happens. Therefore, at both pronation and supination the wing elements closer to the wingtip have a tendency to twist ahead of those nearer to the base and thus create a torsional wave.

of a segment is then

$$\begin{aligned}\tau &= \tau_{gc} + (d_{cm} - d_{gc})(F_y \cos\beta - F_x \sin\beta) + (d_{cm} - d_{ta})(F_y^{insect} \cos\beta - F_x^{insect} \sin\beta)\\ &= I_{cm}(r)\ddot{\beta}. \end{aligned} \tag{6.1}$$

We approximate the wing as having uniform surface mass density. Thus, the moment of inertia of a blade element is $I_{cm} \propto c(r)^3$ at span r. Equation (6.1) determines the pitching motion of each blade element independently of the others. We integrate this equation over pronation and supination to determine how independent blade elements would move based merely on aerodynamic force, and the prescription of the torsion axis motion.

In figure 11, we show the results of integrating (6.1) for the fore- and hind-wings of the dragonfly. We see that if each blade element is allowed to move independently, then the tip of the wing will move ahead of the base. Since a wing is continuous, this will induce a torsional wave along the wingspan during pronation and supination that travels from the wing tip to the base (figure 10).

7. Summary

We have analysed the wing pitch reversal in observed hovering wing kinematics for four different insects. By calculating the rotational power required to pitch the wing using direct numerical simulation and quasi-steady analysis, we have shown that in all these cases, the wing pitch reversal is aided by the aerodynamic torque and wing inertia. The passive wing pitch is consistent with the observed torsional wave which propagates from near the wing tip to wing root. Using a quasi-steady analysis, we identified the main component of the fluid forces that is responsible for the passive wing pitching. We have further determined the relative importance of the aerodynamic and the wing inertial force in these different wing motions.

The observed wing pitching in these cases does not require additional power input from the muscles. This suggests that although insects have the ability to pitch the wing actively, during steady hovering flight, they can benefit from the aerodynamic force and inertia to simplify the control of wing pitching.

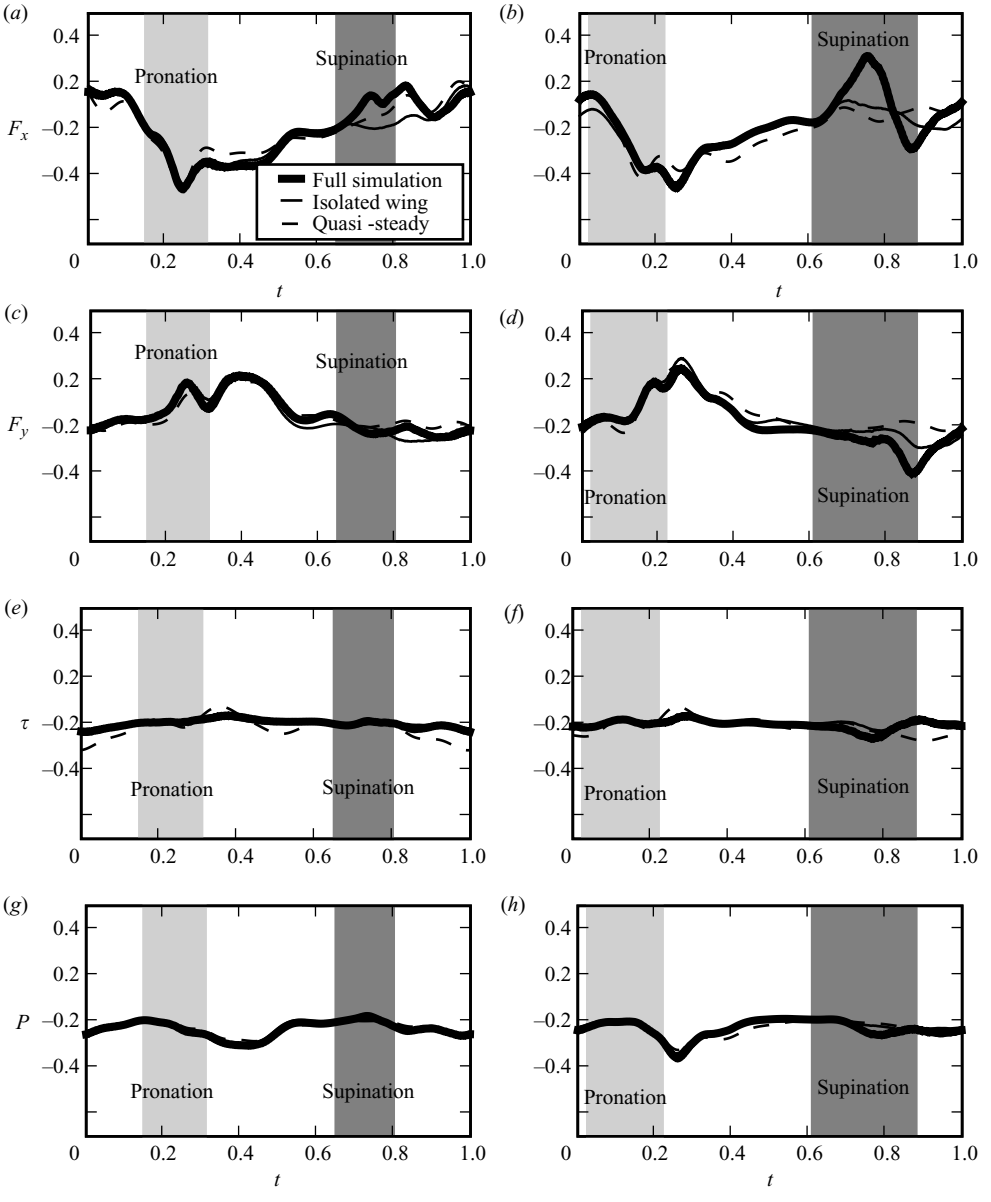

FIGURE 12. Comparison of the quasi-steady model to averaged calculations done using the immersed interface method for dual-wing and single-wing runs for the fore- (a, c, e, g) and hind- (b, d, f, h) wings.

This work is supported by NSF, AFOSR and the Packard Foundation. We thank Gordon Berman and Umberto Pesavento for useful discussions.

Appendix. Comparison of direct simulation to the quasi-steady model

In figure 12, we show a comparison of aerodynamic forces and power as calculated using the immersed interface method and using the quasi-steady model. The parameters are identical to those in § 3.

As can be seen from the figure (with a few notable exceptions which we will discuss below) the predictions using the quasi-steady model are rather close to those from the direct simulations. One difference is the large peak in the drag force (figure 12*e*), and the large dip in lift force (figure 12*f*) during the hind-wing's supination, are missing in the quasi-steady model. Accordingly, the quasi-steady model under-predicts the average drag and over-predicts the average lift. This, in large part, is because both wings generate a net downward jet that is not present in the quasi-steady model. The discrepancies mentioned coincide with the hindwing crossing the shed vortices from the forewing. As expected calculations where the wings are simulated in isolation (also shown in figure 12) do not contain these discrepant features and therefore match the quasi-steady model better. These wing–wing interaction effects make the peaks in figure 5 larger and wing pitch reversal 'more passive'.

REFERENCES

Andersen, A., Pesavento, U. & Wang, Z. J. 2005*a* Analysis of transitions between fluttering, tumbling and steady descent of falling cards. *J. Fluid Mech.* **541**, 91–104.

Andersen, A., Pesavento, U. & Wang, Z. J. 2005*b* Unsteady aerodynamics of fluttering and tumbling plates. *J. Fluid Mech.* **541**, 65–90.

Combes, S. A. & Daniel, T. L. 2003 Flexural stiffness in insect wings ii. Spatial distribution and dynamic wing bending. *J. Exp. Biol.* **206**, 2989–2997.

Dickinson, M. H., Lehmann, F.-O. & Götz, K. G. 1993 The active control of wing rotation by *drosophila*. *J. Exp. Biol.* **182**, 173–189.

Ellington, C. P. 1984 The aerodynamics of hovering insect flight. i. The quasi-steady analysis. *Phil. Trans. R. Soc. Lond.* B **305** (1122), 1–15.

Ennos, A. R. 1988 The inertial cause of wing rotation in diptera. *J. Exp. Biol.* **140**, 161–169.

Fry, S. N., Sayaman, R. & Dickinson, M. H. 2005 The aerodynamics of hovering flight in *drosophila*. *J. Exp. Biol.* **208**, 2303–2318.

Norberg, R. 1972 The pterostigma of insect wings an inertial regulator of wing pitch. *J. Comput. Physiol.* **81**, 9–22.

Pesavento, U. & Wang, Z. J. 2004 Falling paper: Navier–Stokes solutions, model of fluid forces, and center of mass elevation. *Phys. Rev. Lett.* **93** (14), 144501-1–144501-4.

Russell, D. B. 2004 Numerical and experimental investigations into the aerodynamics of dragonfly flight. PhD thesis, Cornell University.

Sane, S. P. & Dickinson, M. H. 2002 The aerodynamic effects of wing rotation and revised quasi-steady model of flapping flight. *J. Exp. Biol.* **205**, 1087–1096.

Sedov, L. I. 1965 *Two-Dimensional Problems in Hydrodynamics and Aerodynamics*. Interscience.

Song, D., Wang, H., Zeng, L. & Yin, C. 2000 Measuring the camber deformation of a dragonfly wing using projected comb fringe. *Rev. Sci. Instrum.* **72**, 2450–2454.

Wang, Z. J. 2000 Two dimensional mechanism for insect hovering. *Phys. Rev. Lett.* **85**, 2216–2219.

Wang, Z. J., Birch, J. M. & Dickinson, M. H. 2004 Unsteady forces and flows in low Reynolds number hovering flight: two-dimensional computations *vs.* robotic wing experiments. *J. Exp. Biol.* **207**, 449–460.

Wang, Z. J. & Russell, D. 2007 The effect of fore and hind-wing interactions on aerodynamic force and power in dragonfly flight. *Phys. Rev. Lett.* (in press).

Weis-Fogh, T. 1973 Quick estimates of flight fitness in hovering animals, including novel mechanisms for lift production. *J. Exp. Biol.* **59**, 169–230.

Willmott, A. P. & Ellington, C. P. 1997*a* The mechanics of flight in the hawkmoth manduca sexta i. Kinematics of hovering and forward flight. *J. Exp. Biol.* **200**, 2705–2722.

Willmott, A. P. & Ellington, C. P. 1997*b* The mechanics of flight in the hawkmoth manduca sexta ii. Aerodynamic consequences of kinematic and morphological variation. *J. Exp. Biol.* **200**, 2273–2745.

Xu, S. & Wang, Z. J. 2006*a* An immersed interface method for simulating the interaction of fluid with moving boundaries. *J. Comput. Phys.* **216**, 454–493.

Xu, S. & Wang, Z. J. 2006*b* Systematic derivation of jump conditions for the immersed interface method in three-dimensional flow simulation. *SIAM J. Sci. Comput.* **27**, 1948–1980.